LETTER

doi:10.1038/nature10751

Structural and functional conservation of key domains in $InsP_3$ and ryanodine receptors

Min-Duk Seo[1]†*, Saroj Velamakanni[2]*, Noboru Ishiyama[1], Peter B. Stathopulos[1], Ana M. Rossi[2], Samir A. Khan[2], Philippa Dale[2], Congmin Li[3], James B. Ames[3], Mitsuhiko Ikura[1] & Colin W. Taylor[2]

Inositol-1,4,5-trisphosphate receptors ($InsP_3Rs$) and ryanodine receptors (RyRs) are tetrameric intracellular Ca^{2+} channels[1]. In each of these receptor families, the pore, which is formed by carboxy-terminal transmembrane domains, is regulated by signals that are detected by large cytosolic structures. $InsP_3R$ gating is initiated by $InsP_3$ binding to the $InsP_3$-binding core (IBC, residues 224–604 of $InsP_3R1$)[2] and it requires the suppressor domain (SD, residues 1–223 of $InsP_3R1$)[2–8]. Here we present structures of the amino-terminal region (NT, residues 1–604) of rat $InsP_3R1$ with (3.6 Å) and without (3.0 Å) $InsP_3$ bound. The arrangement of the three NT domains, SD, IBC-β and IBC-α, identifies two discrete interfaces (α and β) between the IBC and SD. Similar interfaces occur between equivalent domains (A, B and C) in RyR1 (ref. 9). The orientations of the three domains when docked into a tetrameric structure of $InsP_3R$[10] and of the ABC domains docked into RyR[9] are remarkably similar. The importance of the α-interface for activation of $InsP_3R$ and RyR is confirmed by mutagenesis and, for RyR, by disease-causing mutations[9,11,12]. Binding of $InsP_3$ causes partial closure of the clam-like IBC, disrupting the β-interface and pulling the SD towards the IBC. This reorients an exposed SD loop ('hotspot' (HS) loop) that is essential for $InsP_3R$ activation[7]. The loop is conserved in RyR and includes mutations that are associated with malignant hyperthermia and central core disease[9,11,12]. The HS loop interacts with an adjacent NT, suggesting that activation re-arranges inter-subunit interactions. The A domain of RyR functionally replaced the SD in full-length $InsP_3R$, and an $InsP_3R$ in which its C-terminal transmembrane region was replaced by that from RyR1 was gated by $InsP_3$ and blocked by ryanodine. Activation mechanisms are conserved between $InsP_3R$ and RyR. Allosteric modulation of two similar domain interfaces within an N-terminal subunit reorients the first domain (SD or A domain), allowing it, through interactions of the second domain of an adjacent subunit (IBC-β or B domain), to gate the pore.

The essential role of the SD in linking $InsP_3$ binding to $InsP_3R$ gating highlights the need to define the structural consequences of $InsP_3$ binding to the N-terminal region (NT, residues 1–604 of $InsP_3R1$) (Supplementary Fig. 1). Because our attempts to crystallize the NT yielded poorly diffracting crystals, we expressed a Cys-less form of the NT (NT(Cys-less)). Native and Cys-less forms of the NT and IBC behaved indistinguishably (Supplementary Fig. 2 and Supplementary Tables 1 and 2), but NT(Cys-less) provided crystals with diffraction that was much improved (Supplementary Table 3). We determined crystal structures of NT(Cys-less) with (3.6 Å) and without (3.0 Å) $InsP_3$ bound, showing three domains: the SD, IBC-β (residues 224–436) and IBC-α (residues 437–604) (Fig. 1a). The structures of these domains were nearly identical to those of isolated native SD and IBC[2,3] (Supplementary Fig. 3).

The SD, IBC-β and IBC-α form a triangular structure, with the SD behind the $InsP_3$-binding site (Fig. 1a). The SD interacts with the IBC through two interfaces, one with IBC-β (β-interface) and another with IBC-α (α-interface). A 3_{10}-like turn between the last strand of the SD and the first strand of IBC-β positions the IBC relative to the SD (Supplementary Fig. 4e). Within this connecting turn, a salt bridge (between Lys225 and Asp228) stabilizes the backbone conformation and thus positions the residues that form the β-interface. These interactions in the connecting turn and β-interface are augmented by a network of hydrophobic interactions within IBC-β (Fig. 1b). The α-interface forms a long 'Velcro'-like structure that also involves a network of hydrophobic and electrostatic interactions (Fig. 1c). Intimate hydrophobic interactions between Val33, and to a lesser extent Leu32, from the SD; and Val452, Phe445, Ala449 and Leu476 from IBC-α are supported by bidentate salt bridges between Arg54 and Lys127 in the SD and Asp444 in IBC-α (Fig. 1c). The Val33Lys mutation at the α-interface almost abolished inhibition of $InsP_3$ binding by the SD[3,4] and reduced the probability of the channel being open[4]. This confirms the functional importance of the α-interface. Mutation of neighbouring residues that contribute less to the α-interface (Leu32Lys, Asp34Lys, Arg36Glu, Lys127Glu) had less effect on $InsP_3$ binding, and mutation of residues that do not contribute to the interface (Asp35Lys, Lys52Glu) had no effect (Supplementary Table 4)[3,4]. Hydrophobic and electrostatic interaction networks at the α- and β-interfaces contribute to a buried surface between the SD and IBC (~2,040 $Å^2$) that forms a hub connecting $InsP_3$ binding to channel activation.

The structure of the NT is very similar to that of the N-terminal region of RyR1 (ref. 9). The three NT domains of $InsP_3R1$ (SD, IBC-β and IBC-α) can be individually superposed to corresponding domains of RyR1 (A, B and C) (Supplementary Fig. 3). Furthermore, the relative orientation of the three domains within each N-terminal structure is nearly identical (Fig. 1d). Mutation of Tyr167Ala, located on an exposed loop of the SD opposite the IBC interfaces (HS loop[11], residues 165–180, boxed in Fig. 1d), attenuates $InsP_3$-evoked Ca^{2+} release[8], and Ca^{2+}, a co-regulator of $InsP_3R$[13], causes the loop to become accessible[14]. The disease-associated HS loop of RyR1 (ref. 11) sits at the same location within the ABC structure[9] (Fig. 1d), and a mimetic peptide causes RyR2 to become leaky[15]. Furthermore, the backbone and side-chain conformation of this loop region superposes well in the two receptors (Fig. 1e). The HS loop provides a critical link between $InsP_3$ binding and gating.

The domain interfaces of the NT of $InsP_3R1$ and the ABC domains of RyR1 are also similar. The bidentate salt bridges at the $InsP_3R1$ α-interface between Arg54 and Lys127 in the SD and Asp444 in IBC-α are preserved in RyR1 ABC, albeit in a reversed-charge manner between Asp40 and Asp61 in the A domain and Arg402 in the C domain (Supplementary Fig. 4a). In RyR1, mutation of these residues (Arg402Cys, Asp61Asn) is associated with malignant hyperthermia and central core disease[9], suggesting that disruption of the interaction perturbs RyR gating, as it does for $InsP_3R$. The structural similarities

[1]Ontario Cancer Institute and Department of Medical Biophysics, University of Toronto, Ontario M5G 1L7, Canada. [2]Department of Pharmacology, University of Cambridge, Tennis Court Road, Cambridge, CB2 1PD, UK. [3]Department of Chemistry, University of California, Davis, California 95616, USA. †Present address: College of Pharmacy, Ajou University, Suwon 443-749, Korea.
*These authors contributed equally to this work.

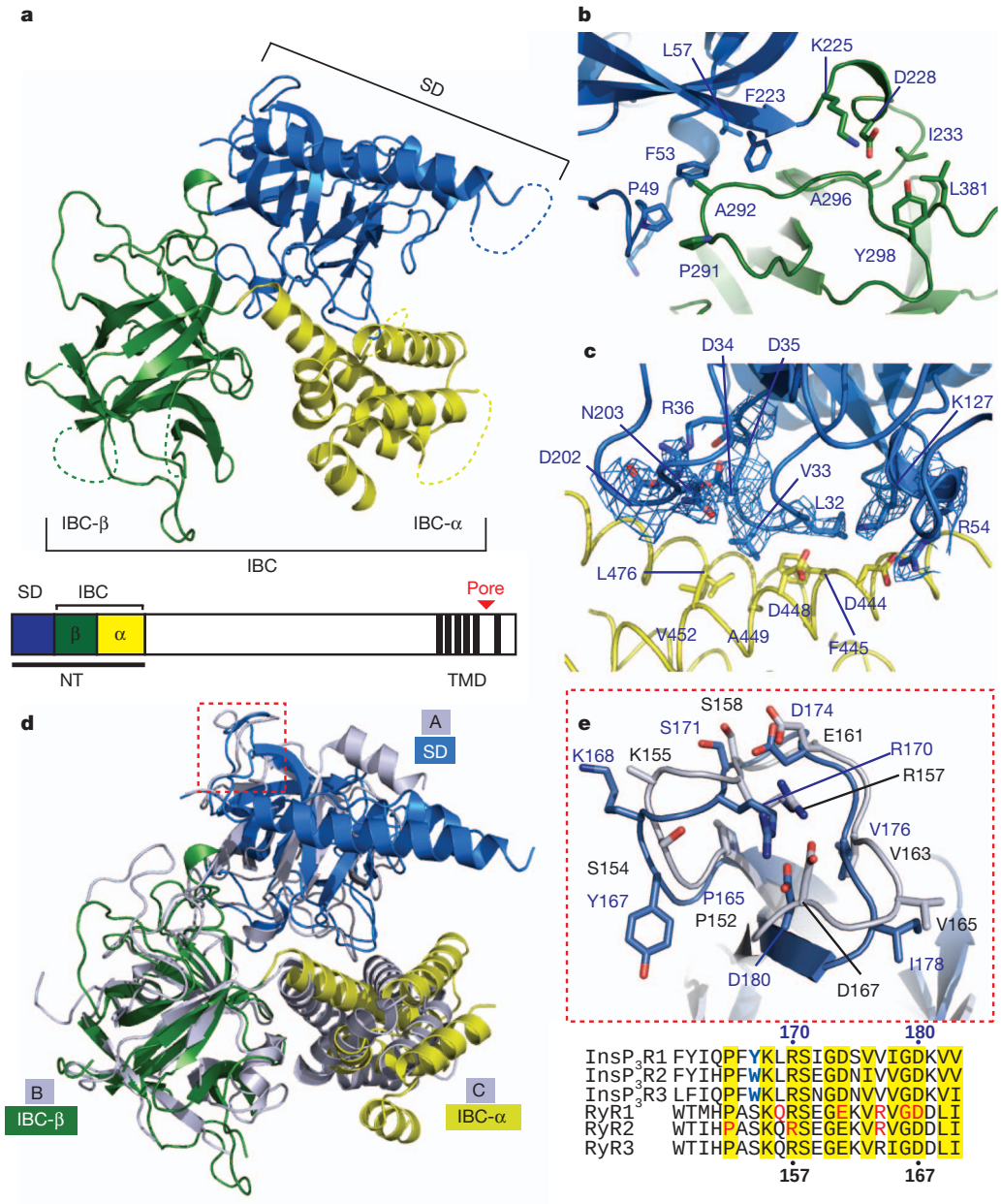

Figure 1 | Structure of the NT region of $InsP_3R1$ without $InsP_3$ bound. **a**, Structure of NT(Cys-less) at 3 Å resolution showing SD (blue), IBC-β (green) and IBC-α (yellow). Dashed lines show invisible regions in the electron density. Positions of the three domains within a single $InsP_3R$ subunit are shown. TMD, transmembrane domain. **b**, **c**, Interfaces between SD–IBC-β (β-interface) (**b**) and SD–IBC-α domains (α-interface, with the hydrophobic core boxed and the $2F_o-F_c$ electron density map of key residues (contoured at 1.0σ) shown as mesh) (**c**). **d**, Superposition of *apo*-NT(Cys-less) and the ABC domain of RyR1 (grey)[9] structures by overlaying IBC-β and the RyR1 B domain. The HS loop in RyR1 and corresponding region in $InsP_3R1$ are highlighted (red box). A, B and C indicate domains of RyR1. **e**, Close-up views of HS regions of $InsP_3R1$ (blue) and RyR1 (grey) with conserved residues depicted as sticks. Structure-based DaliLite alignment of rat $InsP_3Rs$ and rabbit RyRs shows conserved residues (yellow), RyR1 disease-associated mutations (red), and hydrophobic residues that are implicated in activation of $InsP_3R$ (blue)[8].

also extend to the β-interface of $InsP_3R1$ and the corresponding A–B interface in RyR1 (Supplementary Fig. 4b, d). Interestingly, RyR1 forms an additional salt bridge at the A-C interface between Arg45 and Asp447, which is not conserved in $InsP_3R1$ (Supplementary Fig. 4c).

Our structures of NT(Cys-less) with and without $InsP_3$ bound, together with the structure of the $InsP_3$-bound IBC[2] (Supplementary Fig. 5), reveal the structural changes that are evoked by $InsP_3$ (Fig. 2). Side chains of nine residues become organized around $InsP_3$ (Supplementary Fig. 5a), and the domain orientation angle between IBC-β and IBC-α is reduced (by ~8°) after $InsP_3$ binding (Fig. 2 and Supplementary Fig. 5a). This $InsP_3$-evoked 'clam closure', which is consistent with earlier predictions[16] and small-angle X-ray scattering[17], causes the distance across the entrance to the $InsP_3$-binding pocket to decrease (Supplementary Fig. 5b, c). A similar agonist-evoked domain closure occurs in some glutamate receptor channels[18]. The SD and IBC remain associated after closure of the IBC (Fig. 2). $InsP_3$ binding hardly changes the interactions across the extensive α-interface, but at the β-interface the SD residues move away from IBC-β (Supplementary Fig. 5d–f). With the SD glued to IBC-α by the α-interface, and the β-interface serving as a lubricant, $InsP_3$ binding causes the SD to twist (by ~9°) and move closer to the top of the IBC (Fig. 2). This causes an amplified translational movement of the conserved HS loop in the SD (Supplementary Fig. 5g). While our work was under review, 3.8 Å structures of *apo*- and $InsP_3$-bound NT that were derived from a single crystal grown in excess $InsP_3$ were published, showing similar $InsP_3$-induced allostery in the interfaces between domains[19]. This confirms

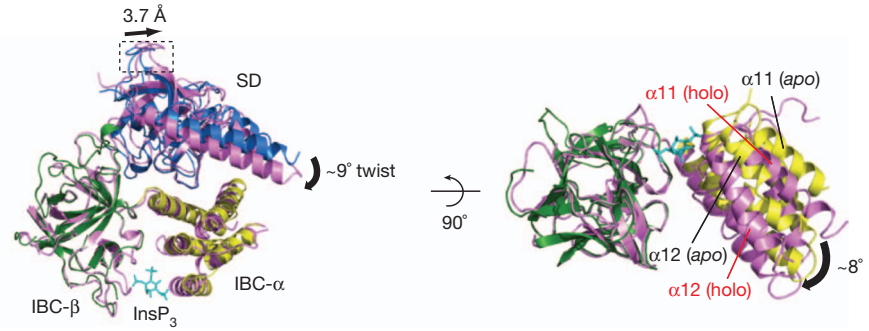

Figure 2 | $InsP_3$-evoked conformational changes. Superposition of *apo*-NT(Cys-less) (SD, blue; IBC-α, yellow; IBC-β, green) and $InsP_3$-bound NT(Cys-less) (3.6 Å resolution, magenta) by overlaying IBC-β domain. $InsP_3$ binding causes the SD to rotate towards the IBC accompanied by a swing that is approximately perpendicular to the IBC 'clam closure'. This twist is measured as the angular difference between the SD arm helices in the *apo*- and $InsP_3$-bound states (~9°). Movement of the HS loop (shown in a dashed box) shows the distance between α-carbons of Tyr 167 (~3.7 Å). A view rotated 90° about the *x* axis is shown (right) with only IBCs represented. The interdomain (IBC-β and IBC-α) angular difference between the free and bound states is ~8°. For further details of $InsP_3$ binding and its effects on the IBC and α- and β-interfaces see Supplementary Fig. 5.

our observations, but our higher resolution structures reveal more detail of the α- and β-interfaces that are associated with this conformational change (Supplementary Discussion).

Docking the ABC structure into cryo-electron microscopy maps of RyR1 showed that the N-terminal domains form a central ring at the top of the mushroom-like RyR1 (ref. 9). Rigid-body docking of our *apo*-NT(Cys-less) structure into a cryo-electron microscope 10 Å structure of a closed $InsP_3R1$ (ref. 10) reveals an arrangement that is remarkably similar to that of RyR1 with a high docking contrast (Fig. 3 and Supplementary Fig. 6). The three domains of the four NTs, which form the upper cytoplasmic surface of the mushroom-like $InsP_3R$, are arranged as four 'hillocks' around a central 'bowl'. This arrangement allows $InsP_3$ unrestricted access to the IBC from the side of the cap (Fig. 3), and it is consistent with accessibility studies and binding sites for regulatory proteins (Supplementary Fig. 6c and Supplementary Table 5). Within the tetrameric $InsP_3R$, the only contacts between NT subunits are through the critical HS loop of the SD and a flexible loop between β-strand 20–β-strand 21 (Supplementary Fig. 7) in IBC-β (Fig. 3c, d). The flexible loop is longer in RyR and it lies ~10 Å further from the neighbouring HS loop[9] (Fig. 3c, d). In $InsP_3R$, the arm domains (residues 67–109) of each SD are the only NT structures that extend beyond the cap towards the pore (Fig. 3a), but these domains are neither essential for $InsP_3R$ activation[8] nor conserved in RyR[9,11].

The structural similarities between the N termini of RyR and $InsP_3R$ prompted us to examine whether the domains are functionally interchangeable. In a chimaeric NT fragment comprising the A domain of RyR2 and the IBC from $InsP_3R1$ (RyR2A-IBC), the A domain mimicked the SD by inhibiting $InsP_3$ binding (Fig. 4a, b). Mutations within the A-domain loop that forms the A–B interface in RyR[9] or the equivalent $InsP_3R$ loop in the SD attenuated this inhibition of binding (Fig. 4c, Supplementary Table 6 and Supplementary Fig. 8). $InsP_3$ stimulated Ca^{2+} release through $InsP_3R1$ or a chimaeric $InsP_3R1$ in which the SD was replaced by the A domain of RyR1 (RyR1A-$InsP_3R1$ (Fig. 4a, d and Supplementary Fig. 9). These $InsP_3Rs$ were similarly expressed and they released similar fractions of the Ca^{2+} stores and had similar sensitivity to $InsP_3$ (Supplementary Table 7). Opening of native $InsP_3R$ or RyR is restrained by interactions between cytosolic domains[20,21]. It is therefore noteworthy that expression of $InsP_3R1$ or RyR1A-$InsP_3R1$ affected neither the Ca^{2+} content of the endoplasmic reticulum nor the Ca^{2+} leak from it (Supplementary Fig. 10), confirming that $InsP_3R$ and RyR1A-$InsP_3R1$ have no detectable spontaneous activity. This demonstrates that the SD of $InsP_3R$ can be functionally substituted by the A domain of RyR.

An $InsP_3R1$ in which residues downstream of transmembrane domain 1 were replaced by the equivalent region of RyR1 ($InsP_3R1$-RyR1) also responded to $InsP_3$ (Fig. 4a, e). Expression of $InsP_3R1$-RyR1 increased Ca^{2+} leakage from the endoplasmic reticulum, and this was reversed by ryanodine, which blocks the RyR pore[22]. However, the increased leak was insufficient to affect the steady-state Ca^{2+} content (Supplementary Fig. 10), suggesting that $InsP_3R1$-RyR1 has minimal spontaneous activity. Expression of $InsP_3R1$-RyR1 matched that of other $InsP_3Rs$, but cells expressing $InsP_3R1$-RyR1 were approximately 20-fold less sensitive to $InsP_3$ (Supplementary Table 7). Because

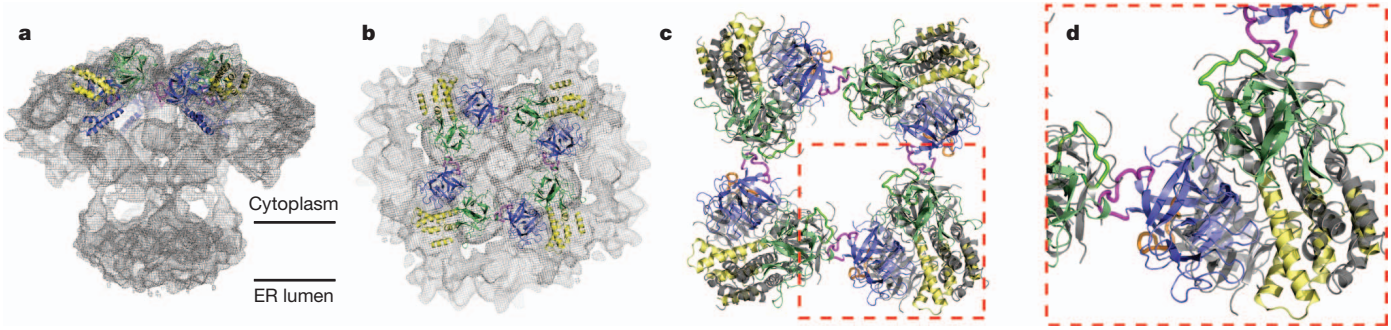

Figure 3 | Docking of the *apo*-NT(Cys-less) structure into the cryo-electron microscopy map of $InsP_3R1$. **a**, **b**, Side (**a**) and top (**b**) views of the *apo*-NT(Cys-less) structure docked into the cryo-electron microscopy map (grey mesh) of $InsP_3R1$ in a closed state[10]. Contour level corresponds to mass of $InsP_3R1$ tetramer of 1.3 megadaltons (MDa) (protein density 0.8 Da $Å^{-3}$). Four molecules of the NT (SD, blue; IBC-β, green; IBC-α, yellow) are located at the top of the cytoplasmic portion of the $InsP_3R1$ tetramer. **c**, Dockings of the *apo*-NT(Cys-less) (coloured as in **a**) and ABC[9] (grey) structures into cryo-electron microscopy structures of $InsP_3R1$ (ref. 10) and RyR1 (ref. 9), respectively, are overlaid and presented to show only NT structures. HS loops of $InsP_3R$ (magenta) and RyR (orange) are highlighted. **d**, Enlargement of boxed area in **c**. Locations of other binding sites within the NT of $InsP_3R1$ are shown in Supplementary Fig. 6.

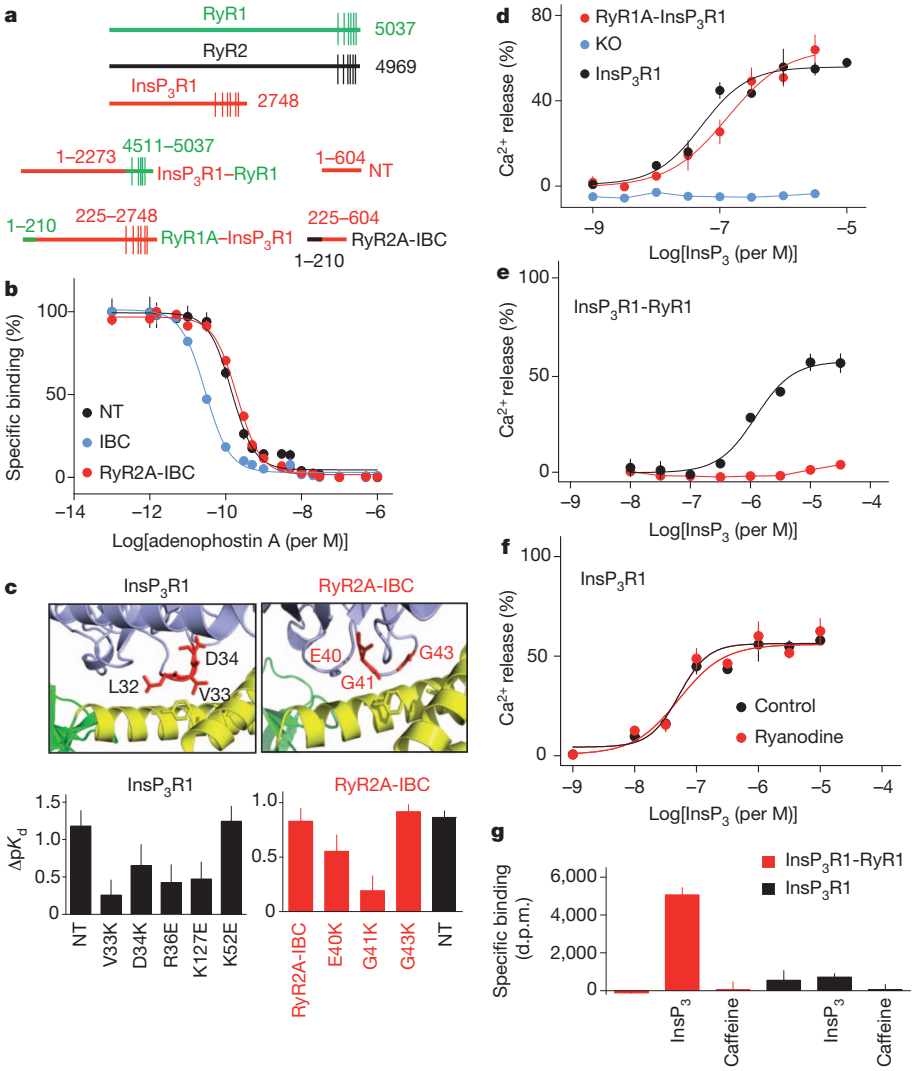

Figure 4 | Functional chimaeras of $InsP_3R$ and RyR. **a**, Proteins used. **b**, Specific binding of ^{3}H-$InsP_3$ in the presence of adenophostin A. **c**, Inhibition of ^{3}H-$InsP_3$ binding to IBC by SD or A domain, and effects of mutations within equivalent loops. Affinities shown relative to IBC (ΔpK_d). The *apo*-NT(Cys-less) (left) and RyR2A-IBC homology (right) structures show key residues (red sticks) within the SD or A domain at the α-interface. The SD/A, IBC-β and IBC-α domains are shown in blue, green and yellow, respectively. **d**, Ca^{2+} release from DT40 cells expressing $InsP_3R1$, RyR1A-$InsP_3R1$ or lacking $InsP_3R$ (knockout (KO)). **e**, **f**, Effect of ryanodine (10 μM) on Ca^{2+} release from DT40 cells expressing $InsP_3R1$-RyR1 (**e**) or $InsP_3R1$ (**f**). Results (**d**–**f**) are percentages of ATP-dependent Ca^{2+} uptake. **g**, Specific ^{3}H-ryanodine binding to membranes of DT40 cells expressing $InsP_3R1$ or $InsP_3R1$-RyR1 with caffeine (10 mM) or $InsP_3$ (1 μM). Nonspecific binding was 2245 ± 211 disintegrations per min (d.p.m.). Results (**b**–**g**) are means ± s.e.m., $n \geq 3$.

the transmembrane domains minimally affect $InsP_3$ binding[23], this diminished response probably reflects a decrease in $InsP_3$ efficacy. The increased Ca^{2+} leakage and reduced efficacy of $InsP_3$ suggest that within $InsP_3R1$-RyR1, communication between the SD and channel are slightly less effective than in native $InsP_3R$. Nevertheless, it is remarkable that cytosolic domains of an $InsP_3R$ should so effectively regulate the pore of a RyR when the two receptors share only modest sequence identity and differ in the number of residues separating the NT from transmembrane domains (Fig. 4a), and in the lengths and sequences of their C-terminal tails and the loops linking transmembrane domains (Supplementary Fig. 11).

Ryanodine (10 μM) had no effect on $InsP_3R1$ or RyR1A-$InsP_3R1$, but it abolished $InsP_3$-evoked Ca^{2+} release through $InsP_3R1$-RyR1 (Fig. 4e, f). Because ryanodine binds selectively to active RyR[24], ^{3}H-ryanodine binding is stimulated by agonists of RyR, such as caffeine. Caffeine had no effect on specific ^{3}H-ryanodine binding to $InsP_3R1$-RyR1, whereas $InsP_3$ stimulated it (Fig. 4g). $InsP_3$ therefore causes conformational changes to the channel of $InsP_3R1$–RyR1 that mimic those of native RyR in allowing binding of ^{3}H-ryanodine. Ryanodine (≤10 μM) did not stimulate Ca^{2+} release through $InsP_3R1$-RyR1 (not shown), suggesting that transmembrane domains alone may not mediate stimulation of RyR[25].

Conservation of structure–function relationships between $InsP_3R$ and RyR (Figs 1–4) allows comparisons between them to suggest possible mechanisms of $InsP_3R$ activation. For both receptors, gating requires conformational changes in the large cytoplasmic structures to pass to the transmembrane domains[10,22], but the N-terminal domains of $InsP_3R$ and RyR are at least 60 Å from these transmembrane domains[1,9,22] (Fig. 3a and Supplementary Fig. 6). Despite some evidence implicating direct interactions between the SD and the loop linking transmembrane domains 4 and 5 in gating $InsP_3R$ (Supplementary Discussion), we suggest, and consistent with results from RyR[20,26,27], that additional cytosolic domains couple the NT to opening of the pore. The exposed HS loop in the SD (Figs 1d and 3c, d) (HS loop of RyR)[9,11] is arranged similarly within the isolated N-terminal structures of $InsP_3R$ and RyR (Fig. 1d) and it reorients after $InsP_3$ binding (Fig. 2). When the NT is docked into the $InsP_3R$ structure[10], the HS loop forms (with an exposed loop of IBC-β) the only interface between adjacent NT regions. However, the equivalent loop is displaced when the ABC is docked into the tetrameric RyR structure[9] (Fig. 3c, d). $InsP_3$ binding closes the

clam-like IBC, disrupting the β-interface and reorienting the HS loop (Fig. 2 and Supplementary Fig. 5). We suggest that this disrupts interaction of the HS loop with a neighbouring NT to cause a coordinated rearrangement of the apical $InsP_3R$ structure (Fig. 3). The open state of RyR1 is associated with outward movement of protein density in regions that match the locations of docked ABC structures[9,22] and with larger movements of peripheral 'clamp domains' (refs 9, 22) that are absent from $InsP_3R$[10]. Movement of these apical domains in RyR is accompanied by rearrangements within regions that taper towards the pore[22] and which, in $InsP_3R$, include the most flexible parts of its structure[10]. We suggest that similar rearrangements of the apical surface of $InsP_3R$ and RyR couple to additional cytosolic domains by shared mechanisms to gate the pore of each channel.

METHODS SUMMARY

The NT residues 1–604 of rat $InsP_3R1$ in which all Cys residues were replaced by Ala (NT(Cys-less)) was expressed in *Escherichia coli* and purified. Crystals of NT(Cys-less) were grown by the hanging-drop vapour diffusion method in 0.1 M HEPES pH 7.0, 0.8–1.0 M $(NH_4)_2SO_4$ and 3% (v/v) trimethylamine N-oxide for *apo*-state crystals, or 0.1 M Na citrate (pH 6.0), 8% (w/v) polyethylene glycol 6000, 70 mM Li_2SO_4 and 3% dimethyl sulphoxide for $InsP_3$-bound crystals. Diffraction data were collected at 100 K on the 19-ID (*apo*-crystals) or 19-BM ($InsP_3$-bound crystals) beam lines at the Advanced Photon Source Synchrotron facility and processed with HKL2000 (ref. 28). Structures of *apo*-NT(Cys-less) at 3.0 Å resolution and $InsP_3$-bound NT(Cys-less) at 3.6 Å resolution were determined by molecular replacement using structures of the SD (Protein Data Bank code 1XZZ)[3] and the IBC (1N4K)[2] as search models with the program Phaser[29]. Iterative refinement and model building were performed with Refmac5 and Coot, respectively. Numbering of secondary structure motifs is in accord with Supplementary Fig. 7. Binding of ^{3}H-$InsP_3$ or ^{3}H-ryanodine to full-length $InsP_3R1$, chimaeras of $InsP_3R1$ and RyR, and to related NT fragments was defined using equilibrium-competition binding assays[4]. Functional properties of $InsP_3R1$ and chimaeras were characterized after stable expression in DT40 cells lacking endogenous $InsP_3R$[4]. A luminal Ca^{2+} indicator was used to record $InsP_3$-evoked Ca^{2+} release from the intracellular stores of permeabilized DT40 cells[4].

Full Methods and any associated references are available in the online version of the paper at www.nature.com/nature.

Received 5 July; accepted 2 December 2011.
Published online 29 January 2012.

1. Serysheva, I. (ed.) *Structure and Function of Calcium Release Channels*. (Academic Press, 2010).
2. Bosanac, I. *et al.* Structure of the inositol 1,4,5-trisphosphate receptor binding core in complex with its ligand. *Nature* **420,** 696–700 (2002).
3. Bosanac, I. *et al.* Crystal structure of the ligand binding suppressor domain of type 1 inositol 1,4,5-trisphosphate receptor. *Mol. Cell* **17,** 193–203 (2005).
4. Rossi, A. M. *et al.* Synthetic partial agonists reveal key steps in IP_3 receptor activation. *Nature Chem. Biol.* **5,** 631–639 (2009).
5. Uchida, K., Miyauchi, H., Furuichi, T., Michikawa, T. & Mikoshiba, K. Critical regions for activation gating of the inositol 1,4,5-trisphosphate receptor. *J. Biol. Chem.* **278,** 16551–16560 (2003).
6. Schug, Z. T. & Joseph, S. K. The role of the S4–S5 linker and C-terminal tail in inositol 1,4,5-trisphosphate receptor function. *J. Biol. Chem.* **281,** 24431–24440 (2006).
7. Chan, J. *et al.* Structural studies of inositol 1,4,5-trisphosphate receptor: coupling ligand binding to channel gating. *J. Biol. Chem.* **285,** 36092–36099 (2010).
8. Yamazaki, H., Chan, J., Ikura, M., Michikawa, T. & Mikoshiba, K. Tyr-167/Trp-168 in type1/3 inositol 1,4,5-trisphosphate receptor mediates functional coupling between ligand binding and channel opening. *J. Biol. Chem.* **285,** 36081–36091 (2010).
9. Tung, C. C., Lobo, P. A., Kimlicka, L. & Van Petegem, F. The amino-terminal disease hotspot of ryanodine receptors forms a cytoplasmic vestibule. *Nature* **468,** 585–588 (2010).
10. Ludtke, S. J. *et al.* Flexible architecture of IP_3R1 by cryo-EM. *Structure* **19,** 1192–1199 (2011).
11. Amador, F. J. *et al.* Crystal structure of type I ryanodine receptor amino-terminal β-trefoil domain reveals a disease-associated mutation "hot spot" loop. *Proc. Natl Acad. Sci. USA* **106,** 11040–11044 (2009).
12. Lobo, P. A. & Van Petegem, F. Crystal structures of the N-terminal domains of cardiac and skeletal muscle ryanodine receptors: insights into disease mutations. *Structure* **17,** 1505–1514 (2009).
13. Taylor, C. W. & Tovey, S. C. IP_3 receptors: toward understanding their activation. *Cold Spring Harb. Perspect. Biol.* **2,** a004010 (2010).
14. Anyatonwu, G. & Joseph, S. K. Surface accessibility and conformational changes in the N-terminal domain of type I inositol trisphosphate receptors: studies using cysteine substitution mutagenesis. *J. Biol. Chem.* **284,** 8093–8102 (2009).
15. Tateishi, H. *et al.* Defective domain-domain interactions within the ryanodine receptor as a critical cause of diastolic Ca^{2+} leak in failing hearts. *Cardiovasc. Res.* **81,** 536–545 (2009).
16. Sureshan, K. M. *et al.* Activation of IP_3 receptors by synthetic bisphosphate ligands. *Chem. Commun.* **14,** 1204–1206 (2009).
17. Chan, J. *et al.* Ligand-induced conformational changes via flexible linkers in the amino-terminal region of the inositol 1,4,5-trisphosphate receptor. *J. Mol. Biol.* **373,** 1269–1280 (2007).
18. Mayer, M. L. Glutamate receptors at atomic resolution. *Nature* **440,** 456–462 (2006).
19. Lin, C. C., Baek, K. & Lu, Z. Apo and $InsP_3$-bound crystal structures of the ligand-binding domain of an $InsP_3$ receptor. *Nature Struct. Mol. Biol.* **18,** 1172–1174 (2011).
20. Hamada, T., Bannister, M. L. & Ikemoto, N. Peptide probe study of the role of interaction between the cytoplasmic and transmembrane domains of the ryanodine receptor in the channel regulation mechanism. *Biochemistry* **46,** 4272–4279 (2007).
21. Ramos-Franco, J., Galvan, D., Mignery, G. A. & Fill, M. Location of the permeation pathway in the recombinant type-1 inositol 1,4,5-trisphosphate receptor. *J. Gen. Physiol.* **114,** 243–250 (1999).
22. Samsó, M., Feng, W., Pessah, I. N. & Allen, P. D. Coordinated movement of cytoplasmic and transmembrane domains of RyR1 upon gating. *PLoS Biol.* **7,** e85 (2009).
23. Iwai, M., Michikawa, T., Bosanac, I., Ikura, M. & Mikoshiba, K. Molecular basis of the isoform-specific ligand-binding affinity of inositol 1,4,5-trisphosphate receptors. *J. Biol. Chem.* **282,** 12755–12764 (2007).
24. Chu, A., Diaz-Munoz, M., Hawkes, M. J., Brush, K. & Hamilton, S. L. Ryanodine as a probe for the functional state of the skeletal muscle sarcoplasmic reticulum calcium release channel. *Mol. Pharmacol.* **37,** 735–741 (1990).
25. Lai, F. A. & Meissner, G. The muscle ryanodine receptor and its intrinsic Ca^{2+} channel activity. *J. Bioenerg. Biomembr.* **21,** 227–246 (1989).
26. Liu, Z. *et al.* Dynamic, inter-subunit interactions between the N-terminal and central mutation regions of cardiac ryanodine receptor. *J. Cell Sci.* **123,** 1775–1784 (2010).
27. George, C. H. *et al.* Ryanodine receptor regulation by intramolecular interactions between cytoplasmic and transmembrane domains. *Mol. Biol. Cell* **15,** 2627–2638 (2004).
28. Otwinowski, Z. & Minor, W. Processing of X-ray diffraction data collected in oscillation mode. *Methods Enzymol.* **276,** 307–326 (1997).
29. McCoy, A. J. *et al.* Phaser crystallographic software. *J. Appl. Crystallogr.* **40,** 658–674 (2007).

Supplementary Information is linked to the online version of the paper at www.nature.com/nature.

Acknowledgements We thank P. Allen and D. MacLennan for gifts of plasmids encoding RyR2 and RyR1, respectively. C.W.T. thanks T. Rahman and V. Konieczny for discussions. M.I. acknowledges K. Mikoshiba and T. Michikawa for long-standing support and discussions. This work was supported by grants from the Heart and Stroke Foundation of Ontario (T-7181) to M.I., National Institutes of Health Research (EY012347 and NS059969) to J.B.A., the Wellcome Trust (085295), the Biotechnology and Biological Sciences Research Council (BB/H009736) and the Medical Research Council (G0900049) to C.W.T. M.-D.S. is supported by postdoctoral fellowships from the Canadian Institutes of Health Research and the National Research Foundation of Korea (2009-352-E00006). A.M.R. is a fellow of Queens' College, Cambridge. M.I. holds a Canadian Research Chair in Cancer Structural Biology.

Author Contributions M.-D.S., N.I., P.B.S., M.I. and C.L. determined and analysed the structure of NT. S.V. prepared and characterized the full-length $InsP_3R$ and chimaeras. A.M.R., S.A.K. and P.D. completed analyses of $InsP_3$ binding and related molecular biology. J.B.A., M.I. and C.W.T. supervised work in their respective laboratories, coordinated the project and, with input from other authors, wrote the paper.

Author Information The atomic coordinates for NT(Cys-less) of rat $InsP_3R1$ with and without $InsP_3$ bound have been deposited in the Protein Data Bank under accession numbers 3UJ4 and 3UJ0, respectively. Reprints and permissions information is available at www.nature.com/reprints. The authors declare no competing financial interests. Readers are welcome to comment on the online version of this article at www.nature.com/nature. Correspondence and requests for materials should be addressed to C.W.T. (cwt1000@cam.ac.uk) or M.I. (mikura@uhnres.utoronto.ca).

METHODS

Materials. $InsP_3$ was from Enzo Life Sciences. Adenophostin A was from A. G. Scientific. Ryanodine was from Ascent Scientific. Cyclopiazonic acid was from Sigma. Sources of other materials are specified in earlier publications[2–4,17] or described below.

Cloning, expression and purification of N-terminal fragments of $InsP_3R1$ and RyR2. The open reading frame (ORF) encoding the NT fragment (residues 1–604) of rat $InsP_3R1$ (GenBank accession number GQ233032.1) was amplified by polymerase chain reaction (PCR) from the full-length clone lacking the S1 splice site using forward 5′-CGGGATCCATGTCTGACAAAATGTCTAGT-3′ and reverse 5′-CGCGCTCGAGTCACTTTCGGTTGTTGTGGA-3′ primers. The PCR product was ligated into a pGEX-6P-2 vector (GE Healthcare) as a BamHI–XhoI fragment to give pGEX(NT), which includes an NT–GST tag followed by a PreScission-cleavage site. To generate NT(Cys-less), a QuikChange multisite directed mutagenesis kit (Agilent) was used to mutate all Cys residues to Ala using pGEX-6P-2-(NT) as the template and using the primers that are listed in Supplementary Table 8. Residues are numbered by reference to rat $InsP_3R1$ containing the S1 splice site.

Plasmids encoding GST-tagged IBC (residues 224–604) and IBC(Cys-less) were generated using PCR to amplify the appropriate sequence from the ORF of full-length rat $InsP_3R1$ or NT(Cys-less) using the following primers: forward 5′-CGGGATCCATGAAATGGAGTAACAAAG-3′ and reverse 5′-CGCGCTCG AGTCACTTTCGGTTGTTGTGGA-3′. Each PCR product was ligated into a pGEX-6P-2 vector as a BamHI–XhoI fragment to produce pGEX-6P-2-(IBC) and pGEX-6P-2-(IBC(Cys-less)), respectively. For analysis of the effects of mutations within the SD on $InsP_3$ binding, the plasmids described previously were used to express His_6-tagged NT and IBC[4] and the His_6-tag was cleaved before experiments[4]. Mutations were introduced using a QuikChange mutagenesis kit and using the primers listed previously[4] or in Supplementary Table 9.

The sequence encoding the A domain of RyR2 was amplified by PCR from rabbit RyR2 (GenBank: GI164831)[30] in pcDNA3 using the primers forward 5′-ACTAGTCTCGAGGTGCTCTTCCAGGGGCCCATGGCTGATGGGGGCG AA-3′ and reverse 5′-GATATCCTTCACTTCCTGAGCTGATGGG-3′. The ORF for the IBC of $InsP_3R1$ was excised from pGEX-6P-2-(NT) as a BamHI–XhoI fragment and ligated into a pET41a vector to produce pET41a-(IBC). To generate a plasmid encoding a chimaeric NT in which the A domain of RyR2 (residues 1–210) was fused to the IBC of $InsP_3R1$ (residues 225–604) (RyR2A-IBC), the PCR product from above was ligated into pET41a-(IBC) as a SpeI–EcoRV fragment to produce pET41a-(RyR2A-IBC). Mutations within the ORF of the A domain of RyR2A-IBC were generated by site-directed mutagenesis using the QuikChange Lightning mutagenesis kit (Stratagene) using the primers listed in Supplementary Table 9. The complete coding sequences of all constructs were confirmed by sequencing. The sequences of the proteins used are summarized in Supplementary Table 1 and Fig. 4a.

For structural studies, NT(Cys-less) was expressed as a GST-fusion protein in BL21-CodonPlus(DE3) *E. coli* strain. Transformed cells were first grown at 37 °C until the $D_{600\ nm}$ reached ~1.0 and they were then induced with 0.5 mM IPTG at 15 °C for ~18 h. Proteins were purified using glutathione sepharose 4B resin (GE Healthcare), and the GST tag was cleaved from the eluted proteins with PreScission protease (GE Healthcare) during overnight dialysis at 4 °C in cutting buffer (20 mM Tris-HCl, pH 8.4, 300 mM NaCl, 5% glycerol and 2 mM DTT). The cleaved proteins were purified further with cation-exchange chromatography (Fractogel EMD SO3- resin, EM Industries) and size-exclusion chromatography (Superdex 200, GE Healthcare). Purified proteins were concentrated to 14 mg ml^{-1} in a buffer comprising 20 mM Tris–HCl, pH 8.4, 360 mM NaCl, 2.5% glycerol, 0.2 mM TCEP (tris(2-carboxyethyl)phosphine), 1 mM PMSF. Similar methods were used to express $InsP_3R$ fragments for binding studies, but with modifications: bacteria were initially grown at 22 °C, the GST tag was cleaved by incubation of bacterial lysates that were immobilized on glutathione sepharose 4B resin with PreScission for 5 h in PreScission-cleavage buffer (GE Healthcare). The eluent was then used for ^{3}H-$InsP_3$ binding analyses without further purification. Western blotting and silver-stained gels were used to verify expression and purification of NT fragments.

Western blot analysis. Western blotting of DT40 cells that were solubilized in Tris-EDTA medium (TEM) containing Triton X100 (1% v/v) was performed as previously described[31] using anti-peptide antisera corresponding to residues 240–253 within the IBC (AbNT, 1:1,000) or 2733–2749 (AbCT, 1:500) of rat $InsP_3R1$. The secondary antibody was HRP-conjugated donkey anti-rabbit antibody (1: 5,000, Santa Cruz Biotechnology).

^{3}H-$InsP_3$ binding. Equilibrium-competition binding assays were performed at 4 °C in TEM (50 mM Tris, 1 mM EDTA, pH 8.3) containing ^{3}H-$InsP_3$ (0.75 nM, Perkin-Elmer Life Sciences), purified protein (1–4 μg) and unlabelled $InsP_3$ in a final volume of 500 μl. After a 5-min incubation, during which equilibrium was attained, reactions were terminated by addition of 500 μl of TEM containing 30% poly(ethylene glycol) 8000 and γ-globulin (750 μg), and centrifugation (20,000*g*, 5 min). For ^{3}H-$InsP_3$ binding to IBC, the amount of ^{3}H-$InsP_3$ was reduced to 0.25 nM, and incubation volumes were doubled. Pellets were solubilized in 200 μl of TEM containing 2% Triton X100 (v/v), mixed with EcoScintA scintillation liquid (National Diagnostics) and radioactivity was determined by liquid scintillation counting. Nonspecific binding was determined in the presence of 10 μM $InsP_3$. Binding results were fitted to a Hill equation (GraphPad Prism, version 5) from which pIC_{50} ($-\log IC_{50}$, in which IC_{50} is the half-maximal inhibitory concentration) and thereby pK_d ($-\log K_d$, where K_d is the equilibrium dissociation constant) values were calculated[32].

^{3}H-ryanodine binding. Microsomal membranes were prepared from DT40 cells by lysis with a glass homogenizer and sonication in cytosol-like medium (CLM) supplemented with protease inhibitors (Roche complete protease inhibitor cocktail), followed by centrifugation (50,000*g*, 30 min). The CLM contained 140 mM KCl, 20 mM NaCl, 1 mM EGTA, 20 mM PIPES, 2 mM $MgCl_2$, 375 μM $CaCl_2$ (free $[Ca^{2+}]$ of ~220 nM), pH 7. Equilibrium-competition binding was performed with microsomal membranes (100 μg protein per ml) at 4 °C in 200 μl of CLM supplemented with protease inhibitors and ^{3}H-ryanodine (100 nM, Perkin-Elmer Life Sciences). Reactions were terminated after 90 min, and radioactivity was determined as described for ^{3}H-$InsP_3$ binding. Nonspecific binding was defined by addition of 10 μM unlabelled ryanodine.

^{3}H-ryanodine binding to RyR typically requires many hours to reach equilibrium[24] because it binds only to the open state of the channel and spontaneous openings are rare. In our analyses of ^{3}H-ryanodine binding to $InsP_3R1$-RyR1 (Fig. 4g), equilibrium was attained within 90 min, perhaps because the modestly increased spontaneous activity of the chimaeric channel (Supplementary Fig. 10b) contributed to an increased rate of ^{3}H-ryanodine binding to the open state. In parallel comparisons, specific binding of ^{3}H-ryanodine to $InsP_3R1$-RyR1 expressed in DT40 cells and stimulated with $InsP_3$ (1 μM) was (d.p.m.: mean (range) for 2 independent experiments): 4,241 (4,073–4,409) after 90 min, 4,941 (4,825–5,058) after 3 h, and 4,410 (4,108–4,712) after 14 h. It is, however, important to note that our conclusion that $InsP_3$ selectively stimulates ^{3}H-ryanodine binding to $InsP_3R1$-RyR1 is not dependent on having measured binding under equilibrium conditions.

Crystallization and data collection. Crystals of *apo*-NT(Cys-less) were grown by the hanging-drop vapour diffusion method at 293 K by mixing 1 μl of protein with an equal volume of reservoir solution (0.1 M Hepes, pH 7.0, 0.8–1.0 M $(NH_4)_2SO_4$). Using an additives screen, 3% (v/v) trimethylamine N-oxide was identified as an important additive to obtain single rod-shaped crystals. After a series of microseeding trials, rod-shaped single crystals were obtained within 5 days. For crystallization of $InsP_3$-bound NT(Cys-less), five molar excess of $InsP_3$ (~1 mM) was added before crystallization. Crystals of $InsP_3$-bound NT(Cys-less) were grown using the same method except for the reservoir solution containing 0.1 M Na citrate (pH 6.0), 8% (w/v) PEG-6000, 70 mM Li_2SO_4 and 3% dimethyl sulphoxide.

For data collection, crystals were equilibrated in 25% glycerol cryoprotective solutions containing reservoir buffer, and flash frozen in liquid nitrogen. Diffraction data were collected at 100 K on a 19-ID beamline for *apo*-state crystals or 19-BM beamline for $InsP_3$-bound crystals at the Advanced Photon Source Synchrotron facility (Argonne National Laboratory), and were processed with HKL2000. Crystals of *apo*-NT(Cys-less) belong to the space group P1 with cell dimension $a = 63.1$ Å, $b = 77.2$ Å, $c = 101.5$ Å, $\alpha = 105.4°$, $\beta = 100.0°$, $\gamma = 101.0°$. Crystals of $InsP_3$-bound NT(Cys-less) belong to the space group *C*2 with cell dimensions $a = 189.2$ Å, $b = 78.7$ Å, $c = 134.1$ Å, $\alpha = 90.0°$, $\beta = 124.5°$, $\gamma = 90.0°$. Crystals of both *apo*- and $InsP_3$-bound NT(Cys-less) contained two molecules in the asymmetric unit (Supplementary Table 3).

Structure determination and refinement. Structures of *apo*-NT(Cys-less) at 3.0 Å resolution and of $InsP_3$-bound NT(Cys-less) at 3.6 Å resolution were determined by molecular replacement using structures of the SD (PDB code 1XZZ)[3] and the IBC (PDB code 1N4K)[2] as search models with the program Phaser[29]. Iterative refinement and model building were performed with Refmac5 (ref. 33) and Coot[34], respectively (Supplementary Table 3). Structures of the two molecules in the asymmetric unit of *apo*-NT(Cys-less) are virtually identical (root mean squared deviation (r.m.s.d.) value = 0.543 Å) except for a minor variation in the loop between β-strand 20 and β-strand 21 that does not affect the interpretation of our results. The low r.m.s.d. between chain A and chain B is maintained through the regions of the molecule that make up the α-interface and β-interface, thus increasing the validity of our description of the 'open-clam' structure. The two molecules in the asymmetric unit of $InsP_3$-bound NT(Cys-less) are more converged than those of the apo-structure (r.m.s.d. value = 0.134 Å), which also validates our description of the 'closed-clam' structure. The molecule of chain A for each state was used to generate figures, but the chain B molecule of *apo*-NT(Cys-less) was used for the side chain of Asp444 in Fig. 1c. All water molecules

were modelled in Coot[34]. Initially, water molecules were detected using the automatic 'find waters' function in the program. A $2F_o-F_c$ map was used with a sigma cutoff value of 1.0, and minimum and maximum distances to protein atoms of 2.4 Å and 3.2 Å, respectively. We subsequently picked additional water molecules and deleted inappropriate water molecules by manually surveying the density in Coot. After refinement, all water molecules exhibiting negative electron density due to inconsistent modelling were deleted.

Circular dichroism analysis. Circular dichroism spectra were collected on a Jasco J-720 spectrometer using a 1-mm path length cuvette at 20 °C. The NT and NT(Cys-less) (0.2 mg ml^{-1}) were prepared in a buffer (20 mM Tris-HCl, pH 8.4, 360 mM NaCl, 2.5% glycerol, 0.2 mM TCEP, 1 mM PMSF). Circular dichroism spectra were obtained from 260 to 200 nm, with a 2-nm bandwidth, an 8-s response time and a scan speed of 50 nm min^{-1}. Data are averages of three consecutive scans.

Cloning and functional expression of chimaeric $InsP_3R$. To generate the plasmid encoding a chimaeric $InsP_3R1$ in which residues 2274–2748 of $InsP_3R1$ (all residues downstream of those immediately before TMD1) were replaced by the equivalent region from RyR1 (residues 4511–5037) ($InsP_3R1$-RyR1), the appropriate region of the ORF of rabbit RyR1 (GenBank accession number X15209)[35] was amplified by PCR from the expression vector pcDNA3.2 using the primers forward, 5′-CGCGGGTTCGAAGTCCCCGAGGCCCCACCAGAACCCCCC-3′, and reverse 5′-CGGGGCGTCCTCGAGTCATTAGCTCAGCTGGTCCTCGTACTGCTTGCGGAAGC-3′. The PCR product was cloned in-frame as a BstBI–XhoI fragment into a pENTR1a vector containing nucleotides 1–6822 of rat $InsP_3R1$. This construct was transferred into the Gateway-compatible expression vector, pcDNA3.2, to generate pcDNA3.2-($InsP_3R1$-RyR1). A plasmid encoding $InsP_3R$ that lacked the SD was generated from ORFs for the full-length $InsP_3R1$ lacking the S1 splice site (pENTR1A($InsP_3R1$)) and the IBC (pENTR1A(IBC)). Both plasmids were digested with NheI and KpnI, and the fragment from pENTR1A(IBC) was cloned into pENTR1A($InsP_3R1$). Site-directed mutagenesis was then used to silence 3 internal BamHI sites within this construct without affecting the coding sequence to generate the plasmid pENTR1A($InsP_3R1^{\Delta SD}$). A plasmid encoding a chimaera in which the SD of $InsP_3R1$ (residues 1–224) was replaced by the A domain of RyR1 (residues 1–210) (RyR1A-$InsP_3R$) was prepared by isolating the coding sequence for the A domain of RyR1 by PCR from the rabbit RyR1 ORF using the primers forward, 5′-GCTAGCATCATGGGTGACGGAGGA-3′ and reverse 5′-GGATCCTTCACAGCAGGAGCAGATG-3′. The PCR product was cloned as a NheI–BamHI fragment into pENTR1A($InsP_3R1^{\Delta SD}$). The complete coding sequences of all plasmids were verified by sequencing. Domain boundaries of the chimaeric proteins are summarized in Supplementary Table 1.

DT40 cells lacking functional genes for native $InsP_3Rs$ (DT40 knockout (DT40-KO)) were transfected by electroporation with linearized plasmids (10 μg DNA per 10^6 cells) using the Neon (Invitrogen) or Amaxa (Lonza) nucleofection systems. G418 (2 mg ml^{-1}) was used to select and amplify clones of G418-resistant cells. Stable cell lines were selected and $InsP_3R$ expression was measured by western blotting. DT40 cells were cultured in RPMI 1640 medium with L-glutamine (Invitrogen) supplemented with 10% fetal bovine serum, 1% heat-inactivated chicken serum (both from Sigma) and 10 μM 2-mercaptoethanol at 37 °C in humidified air containing 5% CO_2. Cells (~2×10^6 cells per ml) were passaged every 2–3 days. Similar methods were used for transient transfections with RyR1 and $InsP_3R1$-NT(Cys-less), but with 50 μg DNA per 3×10^6 cells.

Functional analyses of $InsP_3R$ in DT40 cells. Uptake of Ca^{2+} into the intracellular stores of saponin-permeabilized DT40 cells and its release by $InsP_3$ were measured using a low-affinity Ca^{2+} indicator (Mag-fluo-4) trapped within the endoplasmic reticulum[36]. All experiments were performed at 20 °C in CLM supplemented with 1.5 mM MgATP to allow active Ca^{2+} uptake. After the intracellular stores had loaded to steady state with Ca^{2+} (~150 s), $InsP_3$ was added with thapsigargin (1 μM) to prevent further Ca^{2+} uptake (Supplementary Fig. 9). The effects of $InsP_3$ were assessed after a further 10–40 s. $InsP_3$-evoked Ca^{2+} release is expressed as a fraction of the ATP-dependent Ca^{2+} uptake. Typical experiments are shown in Supplementary Fig. 9.

Structural model of RyR2A-IBC. A structural homology model of RyR2A-IBC (Fig. 4c) was produced using UCSF Chimaera[37] to first superpose the backbone structures of *apo*-NT(Cys-less) and the ABC of RyR1 (PDB, 2XOA), the only RyR subtype for which there is a complete NT structure[9]. This A-domain structure of RyR1 was then used to allow superposition of the A domain from RyR2 (PDB, 3IM5)[12], effectively achieving superposition of NT(Cys-less) onto a 'virtual' chimaera of RyR2A with RyR1BC. The predicted structure of the RyR2A-IBC was then revealed by masking the SD of $InsP_3R1$ and the BC domains of RyR1 (Fig. 4c).

Computational docking. Rigid-body docking of the *apo*-NT(Cys-less) structure into a ~10 Å cryo-electron microscopy density map of $InsP_3R1$ (EMDB, EMDB-5278) was implemented using the six-dimensional search procedure in the Situs Program package[38]. The Laplacian filter was applied to the density maps to enhance the fitting contrast. Docking of the crystal structure of RyR1-ABC (PDB, 2XOA) into a 9.6 Å cryo-electron microscopy density map (EMDB, EMDB-1275), as previously described[9], was repeated using the above procedure. The UCSF Chimera package[37] was used to visualize the docking results with the density maps (Fig. 3 and Supplementary Fig. 6).

30. Otsu, K. *et al.* Molecular cloning of cDNA encoding the Ca^{2+} release channel (ryanodine receptor) of rabbit cardiac muscle sarcoplasmic reticulum. *J. Biol. Chem.* **265,** 13472–13483 (1990).
31. Tovey, S. C. *et al.* Regulation of inositol 1,4,5-trisphosphate receptors by cAMP independent of cAMP-dependent protein kinase. *J. Biol. Chem.* **285,** 12979–12989 (2010).
32. Kenakin, T. P. *Pharmacologic Analysis of Drug–Receptor Interactions* 3rd edn (Lippincott, Williams & Wilkins, 1997).
33. Murshudov, G. N., Vagin, A. A. & Dodson, E. J. Refinement of macromolecular structures by the maximum-likelihood method. *Acta Crystallogr. D* **53,** 240–255 (1997).
34. Emsley, P. & Cowtan, K. Coot: model-building tools for molecular graphics. *Acta Crystallogr. D* **60,** 2126–2132 (2004).
35. Zorzato, F. *et al.* Molecular cloning of cDNA encoding human and rabbit forms of the Ca^{2+} release channel (ryanodine receptor) of skeletal muscle sarcoplasmic reticulum. *J. Biol. Chem.* **265,** 2244–2256 (1990).
36. Tovey, S. C., Sun, Y. & Taylor, C. W. Rapid functional assays of intracellular Ca^{2+} channels. *Nature Protocols* **1,** 259–263 (2006).
37. Pettersen, E. F. *et al.* UCSF Chimera—a visualization system for exploratory research and analysis. *J. Comput. Chem.* **25,** 1605–1612 (2004).
38. Wriggers, W., Milligan, R. A. & McCammon, J. A. Situs: a package for docking crystal structures into low-resolution maps from electron microscopy. *J. Struct. Biol.* **125,** 185–195 (1999).